Enhancing Visible Light Catalytic Efficiency through Modulating Electron Cloud Density via Structure-Function Relationship

*Hong Tu, Yao Tang, Renjiang Guo, Yin Xu, Shengxin Guo, Shunhong Chen, Ya Wang, Yaming Liu, Jian Wu**

National Key Laboratory of Green Pesticide, Key Laboratory of Green Pesticide and Agricultural Bioengineering, Ministry of Education, Guizhou University, Huaxi District, Guiyang 550025, China

Email Address: jwu6@gzu.edu.cn

Keywords: g-C_3N_4, DFT, photo-degradation

Structural modulation of pristine graphitic carbon nitride presents a significant challenge in the rational design of catalysts for efficient degradation of small organic pollutants under visible light. In this study, we combining first-principles calculations and structure-function relationship to predict a high-performance catalyst. The results indicate that CN-8 exhibits a significant degree of separation between electrons and holes, the CN-8 exhibits exceptional degradation efficiency towards rhodamine B, tetracycline and bisphenol A under visible light irradiation. The degradation rate constants are 0.6436 min^{-1}, 0.2432 min^{-1}, and 0.1394 min^{-1} higher than that of bulk g-C_3N_4 (0.0561 min^{-1}, 0.0648 min^{-1}, 0.0232 min^{-1}), respectively. Density functional theory calculations, and structure-function relationship investigations confirm that the superior catalytic activity of CN-8, modifying the amino position changes the electron cloud distribution, promoting efficient separation of photo-generated electron-hole pairs. This study offers valuable insights for developing eco-friendly and efficient photocatalysts for environmental remediation.

1. Introduction

Currently, the escalating issue of water pollution is primarily attributed to industrial sewage discharge, the widespread use of antiviral drugs in the medical field, and agricultural drug use.[1] The presence of emerging pollutants such as pharmaceutical products (tetracycline (TC)), industrial raw materials (bisphenol A (BPA)), pesticides, and dyes (rhodamine B (RhB), methylene blue (MB)) in water systems poses a severe threat to the environment and living organisms.[2-4] Pharmaceutical products, including TC, are commonly used in human and veterinary medicine.[5] When these

pharmaceuticals are excreted or improperly disposed of, they can enter water systems through wastewater treatment plants or runoff from agricultural fields. TC is known to have antimicrobial properties, which can lead to the development of antibiotic-resistant bacteria in the environment. Additionally, TC can disrupt the natural microbial balance in ecosystems, affecting nutrient cycling and overall ecosystem health[6]. Industrial raw materials such as BPA are widely used in the production of plastics and epoxy resins.[7] BPA can leach into water sources from plastic containers, bottles, and cans. It is considered an endocrine-disrupting chemical, meaning it can interfere with hormonal systems in both humans and wildlife. BPA has been linked to various health issues, including reproductive disorders, developmental abnormalities, and certain types of cancers. Insecticide, such as fluralaner (FLLN), are used to control pests agriculture and public health. These chemicals can enter water systems through runoff and leaching from treated fields.[8] FLLN is a broad-spectrum insecticide that targets parasites in animals. However, its presence in water bodies can have detrimental effects on non-target organisms, including aquatic insects, honeybee, and amphibians.[9] Pesticides can disrupt the balance of ecosystems and harm sensitive species, leading to declines in biodiversity. Dyes, such as RhB and MB, are commonly used in industries such as textiles, printing, and paper manufacturing. Discharge of dye-containing wastewater into water systems can result in the contamination of aquatic environments. Dyes can reduce light penetration in water bodies, affecting photosynthesis and disrupting the growth and development of aquatic plants[10]. They can also be toxic to aquatic organisms, causing adverse effects on their survival, reproduction, and overall ecological balance.

Overall, the presence of these emerging pollutants in water systems can have wide-ranging impacts on the environment, including the disruption of ecosystems, harm to living organisms, and potential risks to human health.[11] It is crucial to develop effective methods for their removal and remediation to ensure the protection and sustainability of our water resources. To address this critical challenge, photocatalysis has emerged as a promising strategy for pollutant degradation. However, the low utilization efficiency of sunlight and the high recombination rate of photoinduced charge carriers significantly hinder the overall quantum efficiency and practical applications of photocatalysis.[12] Moreover, there is an urgent need for green and sustainable technologies and policies to effectively mitigate or eliminate the presence of antibiotic residues and dyes in water systems. These stable and nonbiodegradable chemical species, such as RhB, MB, TC, FLLN, and

BPA, have the potential to bioaccumulate and cause adverse effects like endocrine disruption, reproductive anomalies, and eco-toxicity, even in trace amounts in water. Given the demand and stress for clean and potable water, several projects on water reclamation, recycling, and reuse are emerging worldwide.

Semiconductor photocatalysis has shown great potential in degrading aqueous pollutants. Among various semiconductors, graphitic carbon nitride (g-C_3N_4) stands out as a promising inorganic nonmetal conjugated semiconductor. The photocatalytic activity of g-C_3N_4 can be enhanced through various strategies, including doping, functionalization, and structural optimization.[13-14] These approaches aim to modify the electronic structure, surface properties, and structural characteristics of g-C_3N_4, ultimately improving its ability to absorb visible light and facilitate efficient charge separation and transfer. These advancements hold great potential for the development of highly efficient g-C_3N_4-based photocatalysts for environmental applications in pollutant removal from water systems.[15-16] It features a layered graphite-like structure with triazine or heptazine as its basic unit. In recent years, g-C_3N_4 has gained significant attention in the field of photocatalysis due to its excellent physicochemical stability, large surface area, and non-toxicity. Importantly, g-C_3N_4 has a conduction band positioned at -1.4 V and a valence band positioned at 1.3 V, making it highly efficient in absorbing visible light. These unique electronic properties enable g-C_3N_4 to effectively utilize visible light for photocatalytic reactions.[17] Therefore, g-C_3N_4 materials hold great promise for environmental applications in removing pollutants from water.

In this study, we proposed a method to modify the electronic cloud density distribution of the organic conjugated framework through amino modification, which promotes the separation of photo-generated charge carriers. By introducing organic small molecules containing benzaldehyde to pristine g-C_3N_4, the resulting imide structure exhibited an expanded shift in electron cloud density. Previous research has successfully modified the amino group to enhance photocatalytic activity.[18-19] Based on theoretical analysis and literature precedents, we investigated the influence of substituents on the electron cloud density above the benzene ring. Introducing a strong electron-withdrawing group onto the benzene ring enhanced the effective separation of electrons and holes. Our team utilized Density Functional Theory (DFT) to compute the first excited state (S1) electron-holes distribution patterns of twelve unique functional groups and S1~S5(first excited state to fifth excited state) electron-holes distribution of CN-8 and g-C_3N_4 supercell (Figure 1).[20] This

method effectively enhances the conjugation of pi-pi bonds and increases the separation distance of electron-hole pairs, leading to significantly enhanced photocatalytic activity. This study proposes, for the first time, the reliable verification of the structure-function relationship by using DFT to calculate electron-holes.[21]

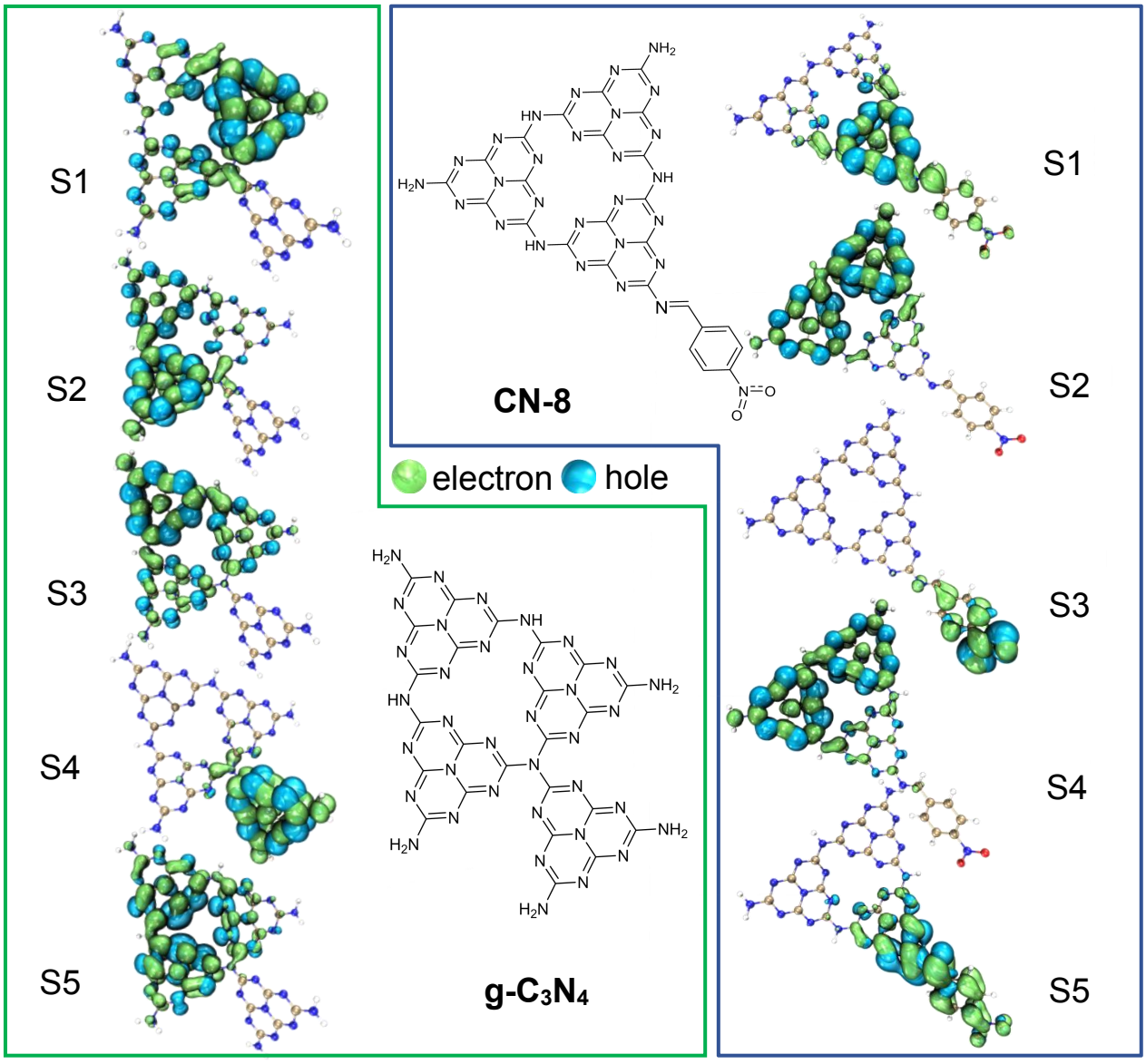

Figure 1. The electron-holes distribution of the first to fifth excited states in g-C_3N_4 and CN-8 calculated by DFT calculations.

2. Results and Discussion

2.1 Preparation and characterization of photocatalysts

To prepare a highly active CN-8 catalyst with enhanced light absorption, a temperature gradient selection approach was employed during the synthesis of g-C_3N_4. It was found that temperatures below 520 °C resulted in insufficient urea polymerization, while higher temperatures (590, 600, 610 °C) led to low yields.[22-23] Therefore, g-C_3N_4 precursor materials were prepared at 520, 550, and 580 °C. Infrared spectroscopy revealed an increase in ─C=N (1660-1680 cm^{-1}) bonds with increasing temperature (**Figure 2**i). Among the synthesized materials, CN580 exhibited the best degradation activity towards RhB under visible light at 450 nm. CN580 was further modified using 12 different benzaldehyde derivatives connected to the phenyl ring, resulting in the synthesis of CN-1 to CN-12.[24] After modifying CN580 with p-nitrobenzaldehyde to obtain CN-8, the infrared spectra showed the disappearance of hydrogen bonds formed by amino groups absorption peak (3620-3680 cm^{-1}).[25] Density functional theory (DFT) calculations, combined with experimental screening, identified CN-8 as the most suitable catalyst. The SEM images shown in **Figure S1**(Supporting Information) indicate that CN520, CN550, CN580, and CN-8 have a 2D plate structure due to strong π–π stacking, while HRTEM images (Figure 2) show that they have a transparent sheet-like morphology. However, the selected area electron diffraction (SAED) pattern (**Figure 2**c, inset) does not show any lattice fringes, suggesting that CN-8 is amorphous.[26]

To analyze the crystal structure of CN520, CN550, CN580, and CN-8, we examined their X-ray powder diffraction (XRD) patterns (**Figure 2**j). These patterns revealed two distinct diffraction peaks at 13.1° and 27.3°, corresponding to the (100) in-plane long-range atomic order and (002) interlayer-stacking motif, respectively.[27] As the calcination temperature of g-C_3N_4 increased, we observed an increase in the intensity of the (002) peak, indicating an improvement in the stacking order of the interlayers. This suggests that higher calcination temperatures promote the formation of a more ordered crystal structure. Furthermore, when comparing the modified sample (CN550-8) to CN550, we observed a significant increase in peak intensity.[28] This indicates that the modification with electron-donating groups at the amino position (CN-8) enhances the crystallinity of the material, leading to a more organized and stable structure. This enhancement in crystal structure may contribute to the improved photocatalytic performance observed in the degradation experiments. Overall, these XRD results provide strong evidence for the structural changes induced by the modification of g-C_3N_4 and highlight the potential of these modified materials for various applications.

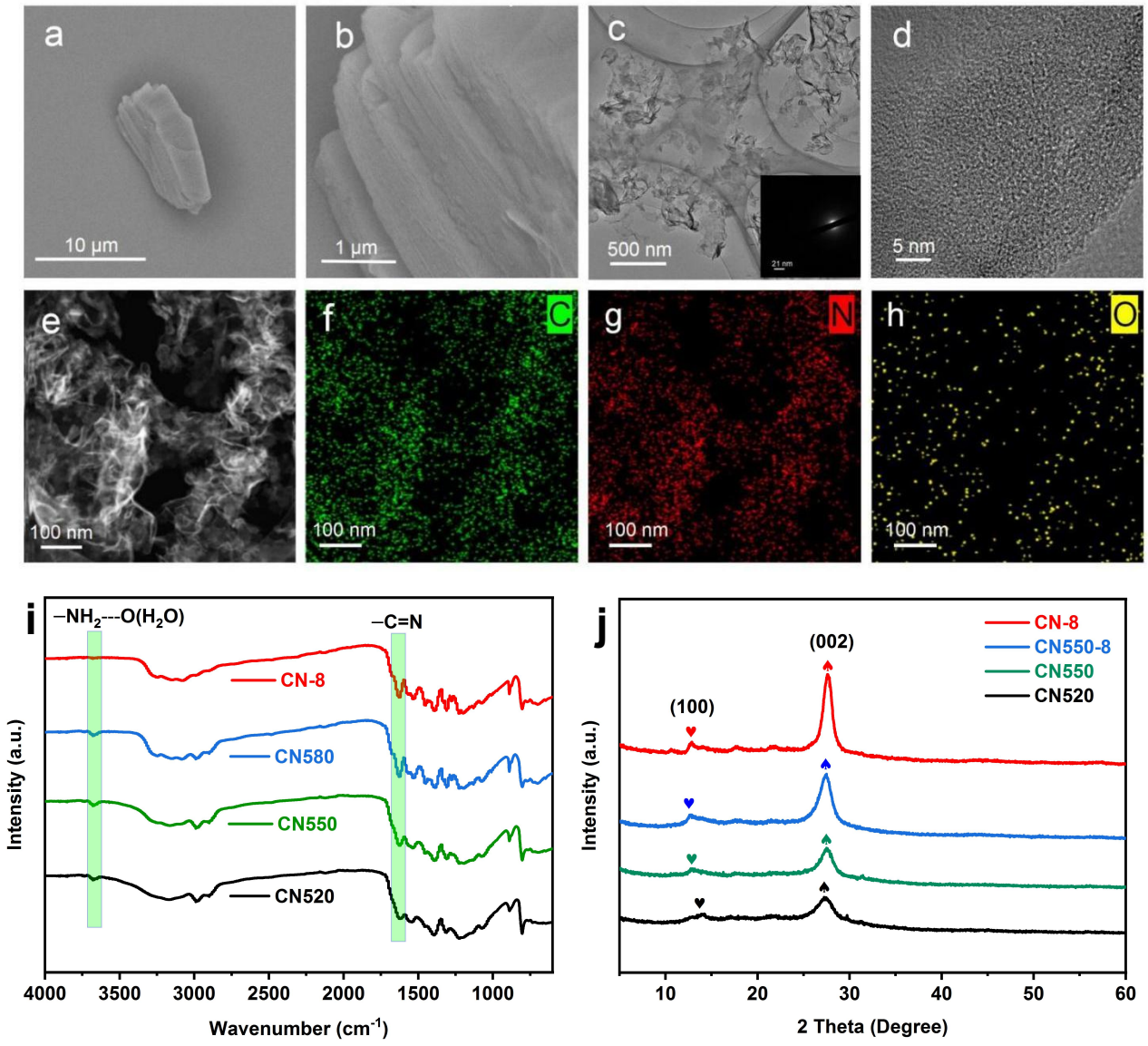

Figure 2. (a-b) SEM and (c–e) TEM images of CN-8, (f-h) the corresponding elemental mapping on C, N, and O. (i) FT-IR for CN520, CN550, CN580, and CN-8. (j) XRD for CN520,CN550, CN550-8, and CN-8.

To verify the structural change in CN520, CN550, CN550-8, and CN-8, Fourier transform infrared (FTIR) spectroscopy was performed. The absorption peak of the –C=N bond (1620-1680 cm^{-1}) increases with the increase of the calcination temperature of g-C_3N_4, as shown in the **Figure 2**i. The –NH_2 stretching vibration peak of the N–H bond and hydrogen bonds between molecules are located at 3620-3680 cm^{-1} for CN520, CN550, and CN580. The disappearance of this absorption peak in the CN-8 sample indicates successful modification of the amino group. These peaks demonstrate that benzaldehyde-type compounds have been successfully introduced into the framework of g-C_3N_4.

To better understand the structure and surface chemical properties of CN-8, we conducted X-ray photoelectron spectroscopy (XPS) characterizations. Both XPS survey spectrum and O 1s spectrum with binding energy at 532.6 eV indicate the introduction of p-nitrobenzaldehyde (**Figure 3**c).[29] As shown in **Figure 3**d-i and Supplementary Table 4, the C 1s and N 1s spectra exhibit

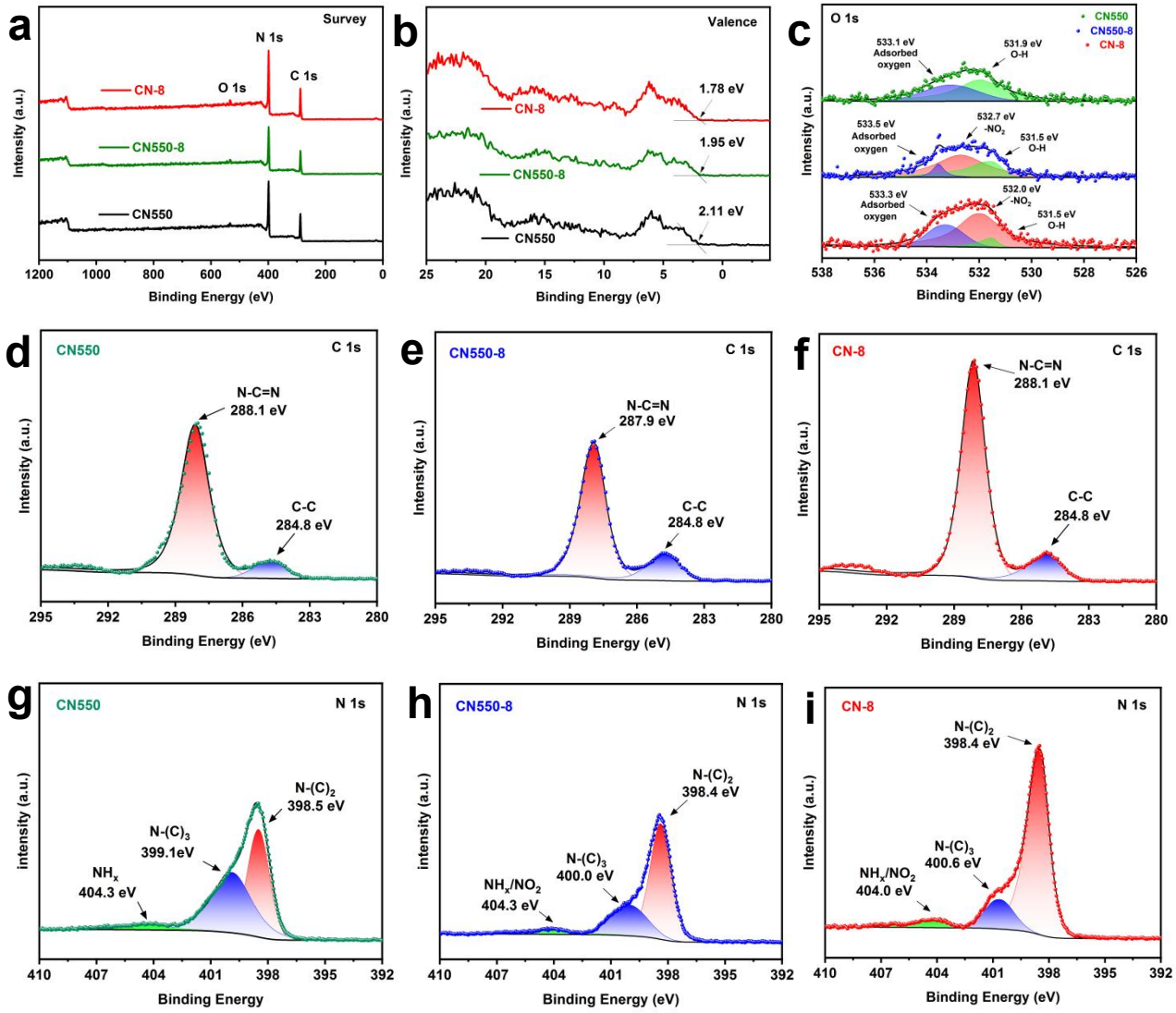

Figure 3. (a) XPS survey for ,CN550, CN550-8, and CN-8. (b) XPS valence for CN550, CN550-8, and CN-8. (c-i) XPS of O 1s (c), C 1s (d-f) , and N 1s (g-i).

characteristic peaks of C and N heterocycle frameworks. Specifically, the N=C–N, N–$(C)_2$, and N–$(C)_3$ peaks are observed at 288.1, 398.4, and 400.6 eV, respectively.For CN-8, the higher binding energies of the C 1s, N 1s, and O 1s are associated with the structural change modified by the p-nitrobenzaldehyde. It is notable that the integrated peak area ratio N-$(C)_2$ in N 1s is significantly increased from 13.03 % (CN550) to 22.45 % (CN-8)(Table S4).[30]

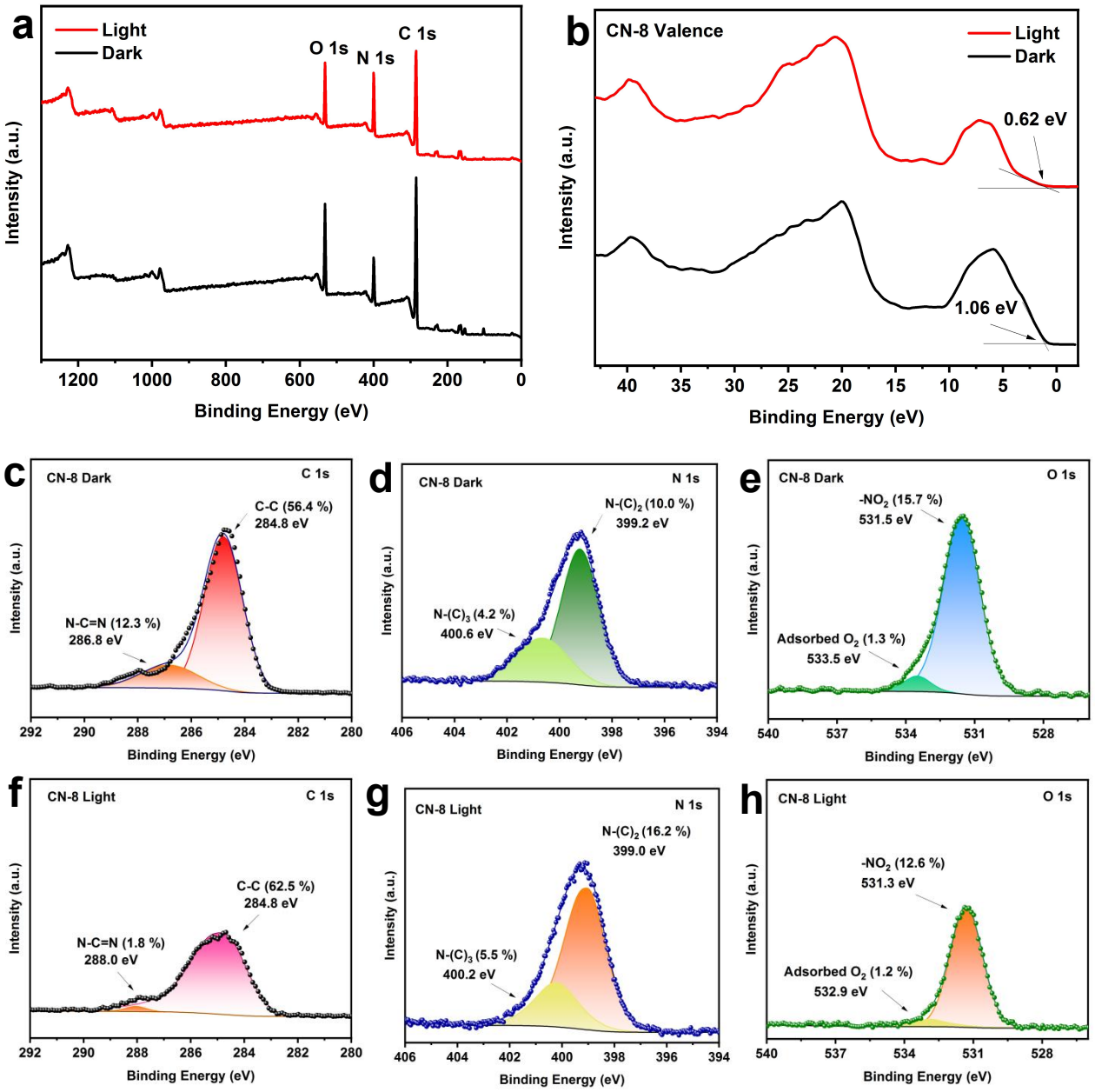

Figure 4. The XPS analysis of CN-8 was performed under an N_2:O_2 atmosphere ratio of 8:2, including measurements under dark and 5-minute light conditions.

From **Figure 4**, it is evident that the surface elemental bands of CN-8 undergo significant changes under dark and light conditions. In the C 1s spectrum, the C-C peak at 284 eV increases from 56.4% to 62.5%, while the N-C=C content decreases from 12.3% to 1.8%. In the N 1s spectrum, the N-$(C)_2$ peak increases from 10% to 16.2%, and N-(C)3 increases from 4.2% to 5.5%. The O 1s spectrum shows a decrease in -NO_2 content from 15.7% to 12.6%. Additionally, the valence band decreases from 1.06 eV under dark conditions to 0.62 eV. These findings suggest

significant surface modifications and potential enhancements in the photocatalytic performance of CN-8.[31]

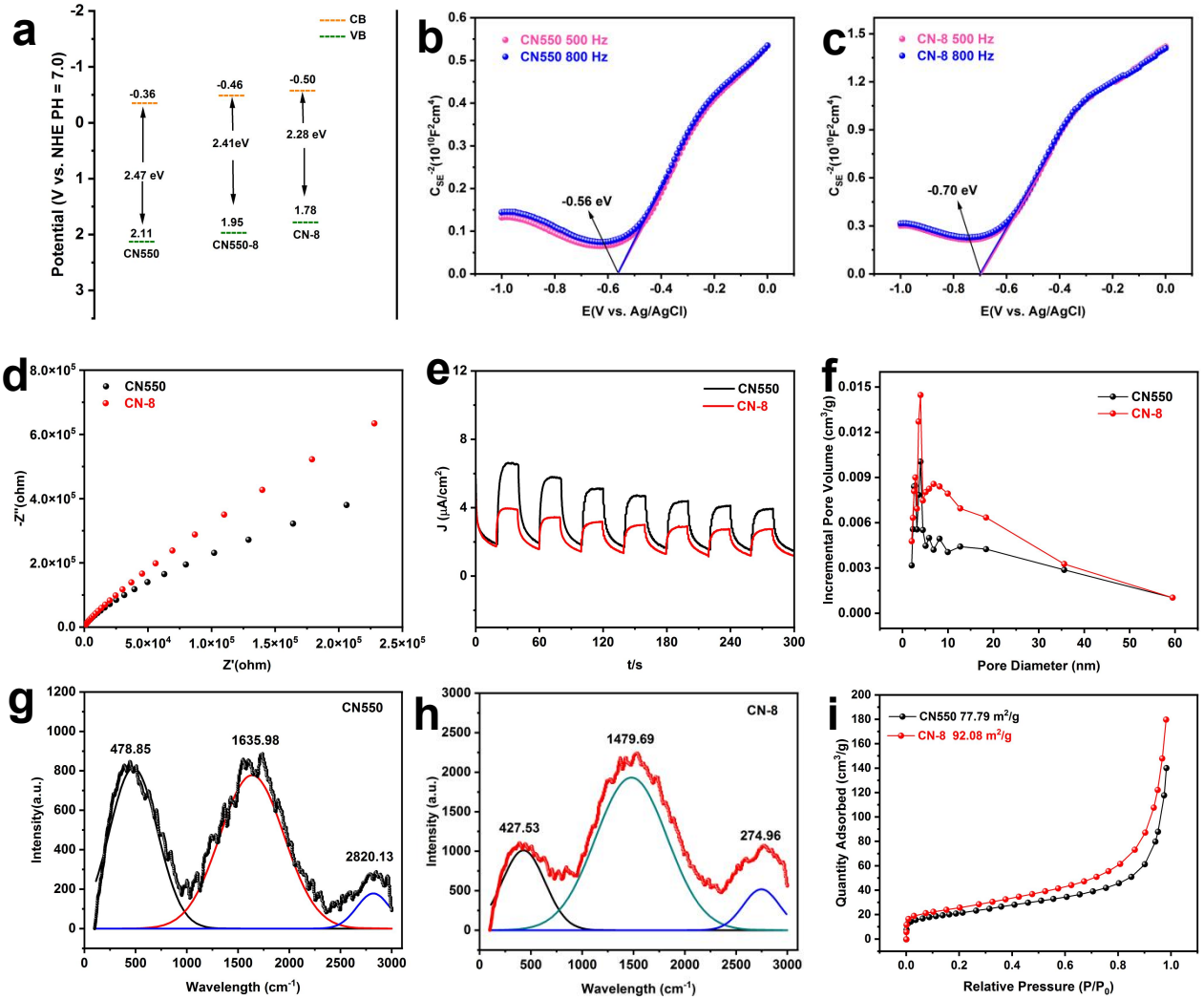

Figure 5. (a) Band structure alignments. (b-c) Mott-Schottky plots of CN550 and CN-8. The potential values in these figures can be converted to potential relative to the standard hydrogen electrode (NHE) using the formula: E (NHE) = E (Ag/AgCl) + 0.197 V. (d) Nyquist plots periodic of CN550 and CN-8 from Electrochemical impedance spectroscopy. (e) ON/OFF photocurrent response. (f) The BJH pore size distributions and (i) N_2 adsorption isotherms of CN550 and CN-8. (g-h) Raman spectrum of CN550 and CN-8.

The amino modification and variation in calcination temperature significantly impact the optical properties and light absorption capabilities. From UV-vis DRS shows that CN-8 demonstrates a stronger and red-shifted absorption capacity compared to CN550 (**Figure S2**a). The calculated Kubelka-Munk function reveals a progressively narrowed, direct bandgap from 2.49 eV in CN550 to 2.05 eV in CN-8 **(Figure S2**b). The flat band potentials estimated from the measured

Mott-Schottky plots are directly employed as the conduction band (CB) edge potentials (**Figure 5**b-c, **Figure S**3). From XPS valence band (VB) edge potentials of CN550 and CN-8 are estimated as 2.11 and 1.78 eV, respectively(**Figure 3**b), establishing the band structure alignments in **Figure 5**a. Charge transfer and separation in CN-8 are further elucidated through steady-state and time-dependent photoluminescence (PL) measurements. The PL spectra (**Figure 6**b) confirm a red-shift in CN-8, indicating a reduced bandgap.

By fitting a double exponential equation (**Figure 6**a; Table S5), it was found that the electron/hole recombination lifetimes of CN520 were relatively short, but after high-temperature calcination and modification with dinitrobenzaldehyde at the amino sites, the electron/hole recombination lifetimes of the material were significantly improved. Considering the longer PL lifetime, CN-8 was considered the optimal choice. The photocatalytic performances of CN550 and CN-8 were investigated using electrochemical impedance spectroscopy (EIS) **(Figure 5**d). By comparing CN-8 to CN550 (**Figure 5**e), indicating its weak electron transfer ability and efficient separation of photogenerated carriers for photocatalysis. It can be observed from the graph that the differences in amino modification and calcination temperature resulted in changes in the electron transfer pathways, thereby affecting the intensity of the photoresponse signal. As shown in **Figure 5**i and Table S5, CN550 and CN-8 exhibit type IV isotherms owing to the presence of abundant mesopores. The CN-8 catalysts exhibit much higher specific surface areas and porosities than CN550 up to 92.07 $m^2g^{-1}$and 0.2785 cm^3g^{-1}, which is beneficial for facilitated mass diffusion kinetics during catalysis. The Raman spectroscopy test reveals that CN-8 exhibits a broader peak width and relatively lower peak position, indicating the presence of lattice defects and distortions in its structure. In contrast, CN550 demonstrates higher peak positions and narrower peak widths, suggesting a more intact and stable lattice structure (**Figure 5**g-h).[32]

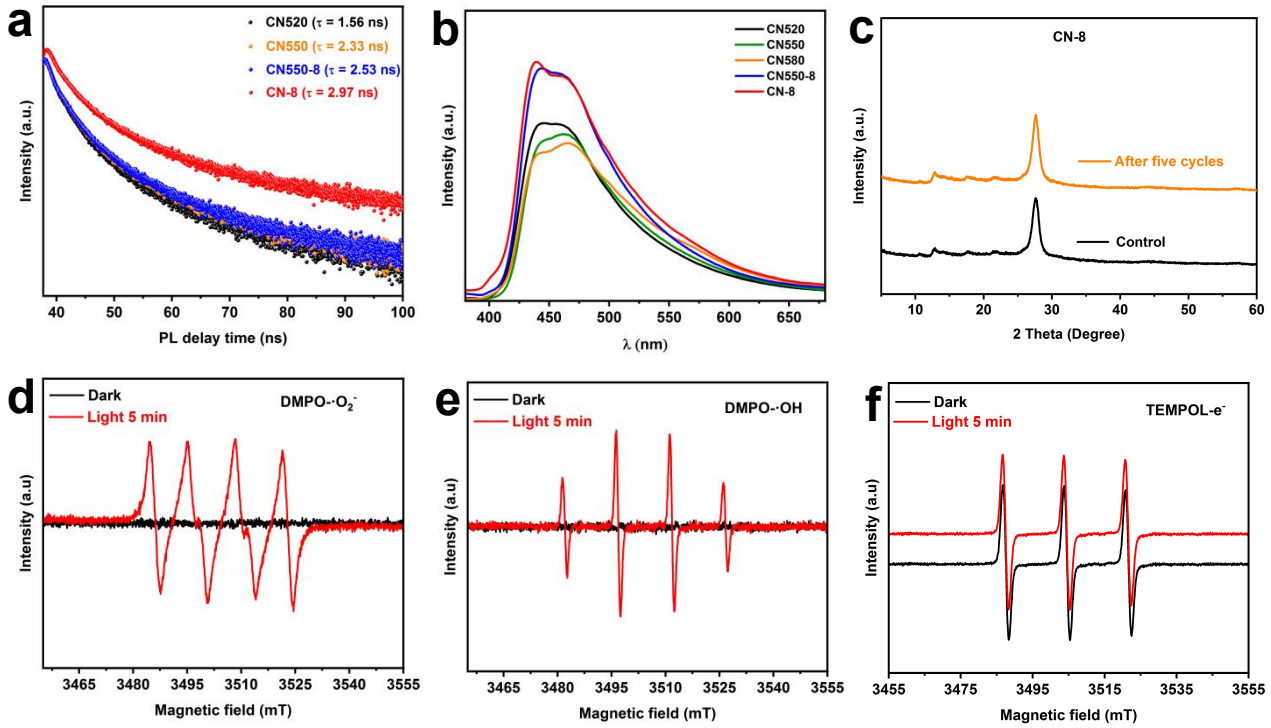

Figure 6. (a) Time-resolved photoluminescence spectra of CN520, CN550, CN550-8, and CN-8. (b) Steady-state PL spectra of CN520,CN550, CN580, CN550-8. (c) XRD comparison between original CN-8 and CN-8 after 5 cycles. (d-f) EPR of $\cdot O^{2-}$, $\cdot OH$, and e^- under dark and light conditions.

2.2 DFT calculation

To gain a deeper understanding of the relationship between amino modification and the distribution of electrons and holes, we conducted first-principle density functional theory (DFT) calculations. After optimizing the structure and performing single-point energy calculations, we analyzed the energy of the first excited state. By plotting the distribution of electrons and holes in the first excited state and comparing it with the experimental rates of RhB photocatalytic degradation (**Figure 7**a-c; Table S3), we observed that higher proportions of electrons and holes on the modified fragments corresponded to higher catalytic rates. Among them, CN-8 and CN-9 exhibited the highest proportion of electron holes. We further investigated the bond lengths between N and O in the modified fragments (**Figure S4**) and found that CN-8 had longer bonds, facilitating better separation of electrons and holes (**Figure 8**).

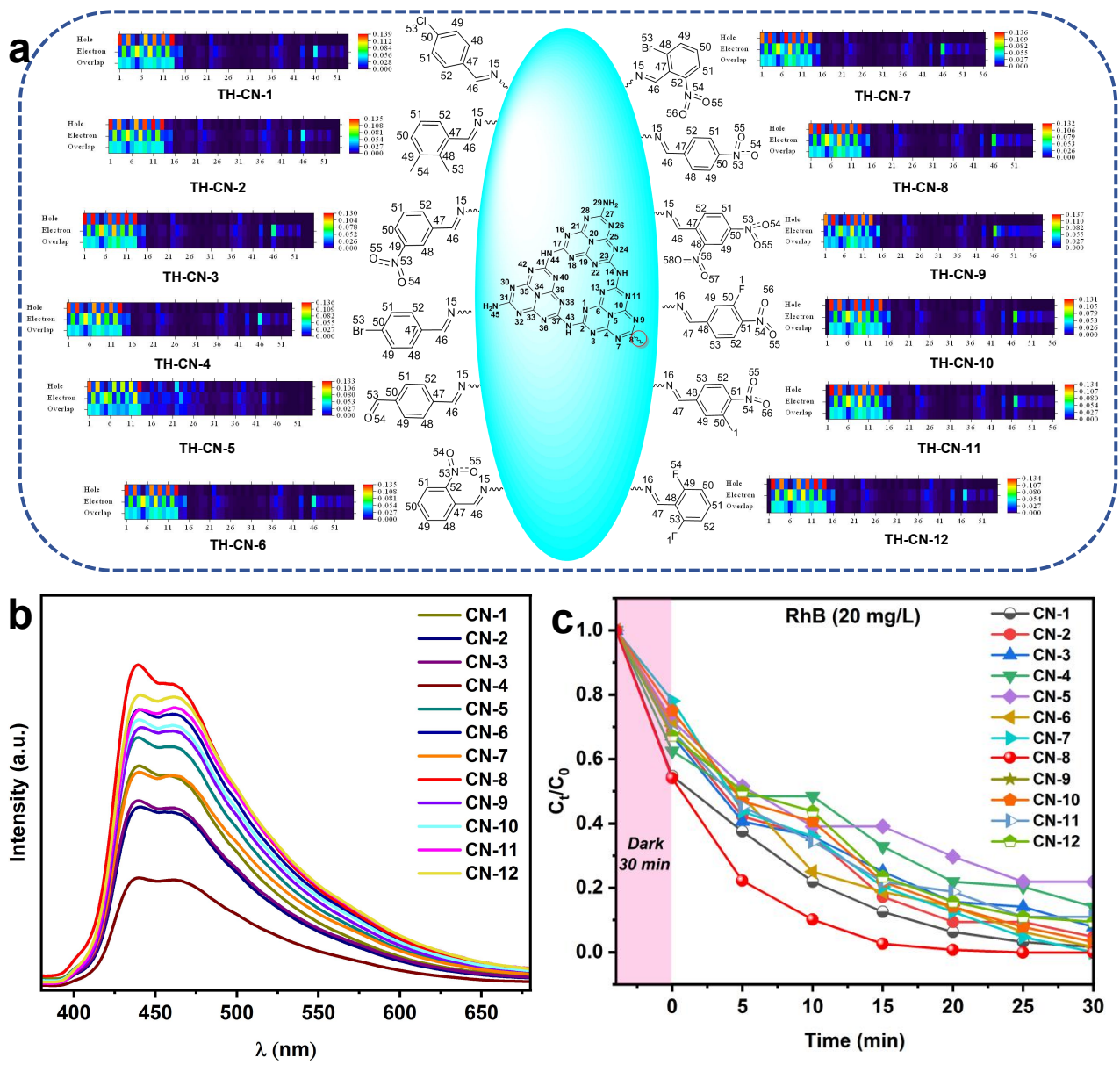

Figure 7. (a) The chemical structures and S1 electron-holes distribution hot-maps of CN-1~CN12. (b) Steady-state PL spectra of CN-1~CN12. (c) Time curves of degradation of RhB by CN-1~CN-12 under the irradiation of a 6 W LED lamp at λ = 450 nm.

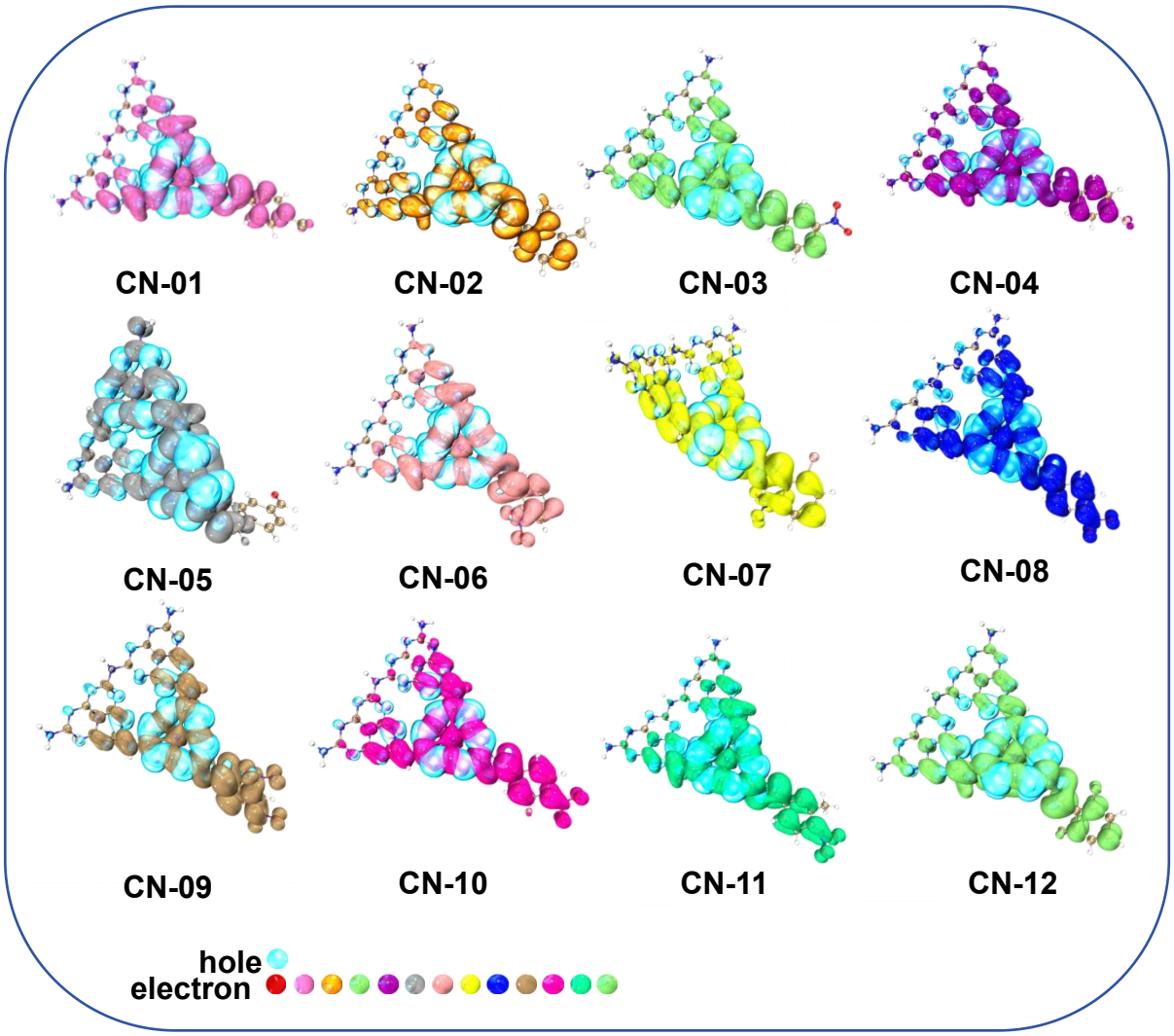

Figure 8. Visualization of the First Excited State electron-holes in CN-1~CN-12.

2.3 Degradation mechanism

A reasonable reaction mechanism has been proposed in **Figure 10**a, taking into account the aforementioned studies. In neutral conditions (pH 7), electrons and holes are generated on the CN-8 surface through efficient absorption of visible light, leading to charge separation. Oxygen molecules are activated by nearby electrons, resulting in the generation of a significant quantity of $\cdot O_2^-$ anion radicals through the one-electron reduction of oxygen ($E(O_2/\cdot O_2^-) = -0.33$ V vs. NHE, as represented by **Text S**1 Equation (1), Supporting Information).[33]

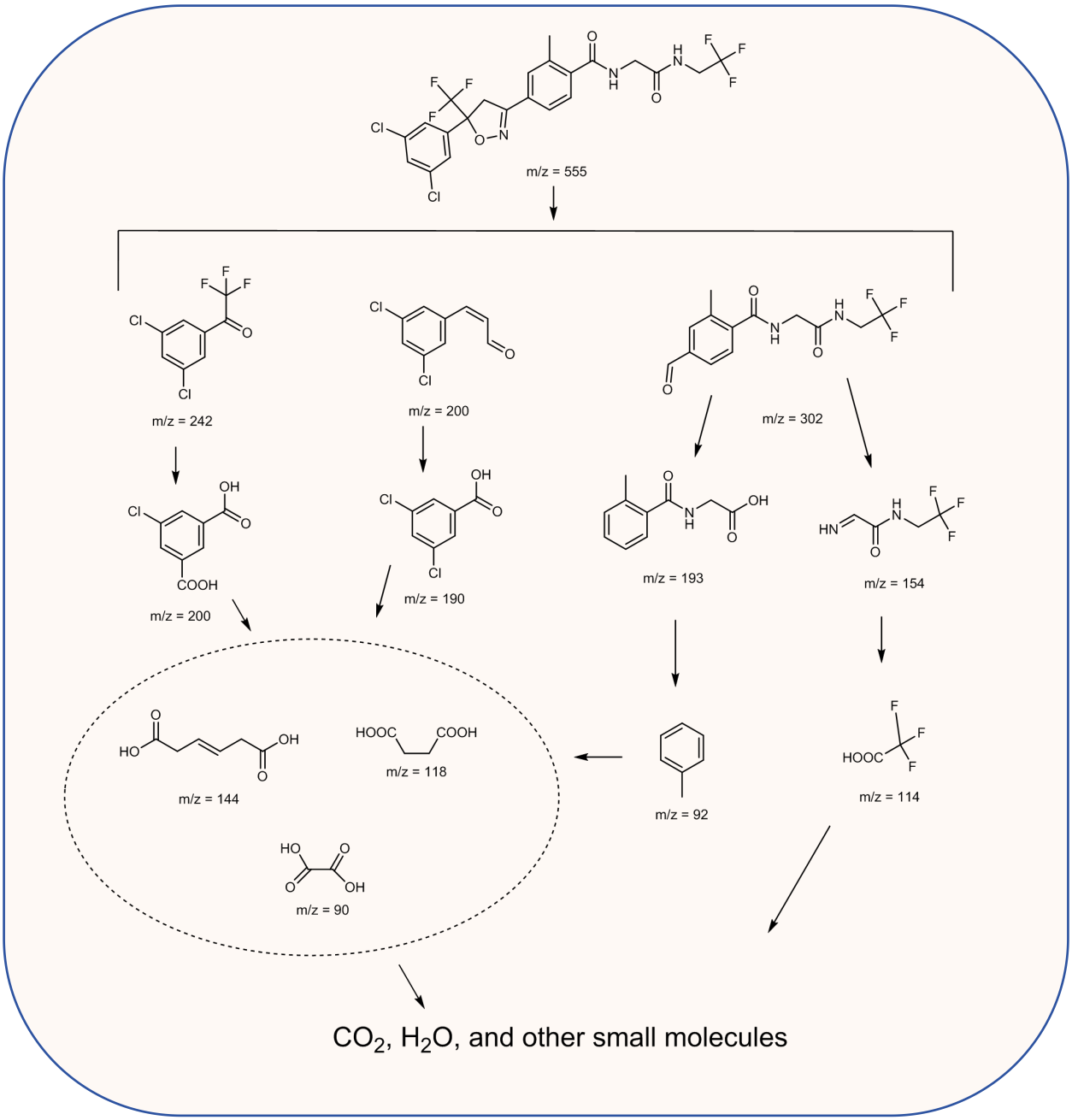

Figure 9. Possible degradation pathways of FLLN inferred from LC-MS analysis.

This process is feasible because the CB edge potential of CN-8 (−0.50 V vs. NHE, **Figure 5**a) is more negative than the redox potential. Since the VB edge potential of CN-8 (+1.78 V vs. NHE) is less positive than the redox potential of $H_2O/\cdot OH^-$(+2.40 V vs. NHE, Text S1 Equation (2), Supporting Information), It is difficult to generate ·OH radicals on CN-8 through a direct oxidation of OH^- or H_2O by h^+. The $\cdot O_2^-$ anion radicals can abstract another e^- to produce intermediate, H_2O_2 (the redox potential of $\cdot O_2^-/H_2O_2$ is 0.94 V vs NHE, Text S1 Equation (3), Supporting

Information).[34] Subsequent one-electron reduction of H_2O_2 leads to the generation of ·OH radicals indirectly (the redox potential of H_2O_2/·OH is 0.32 V vs NHE, Text S1 Equation (4), Supporting Information). From the comparison in band structure alignment between CN-8 and CN550, we conclude that the separation of electrons and holes caused by modification of the amino site are esential for such direct and indirect generation of reactive species(Text S1 Equation (1-9), Supporting Information). After LC-MS analysis, the possible degradation pathway of FLLN is illustrated in **Figure 9 (**FLLN LC-MS analysis, Supporting Information**).** We conducted bio-toxicity tests before and after FLLN degradation, and the results revealed a reduction in toxicity by over 95% following degradation (**Figure S13**). The mineralization rates of organic pollutants RhB, MB, TC, BPA, and FLLN, under 12 W LED λ = 450 nm illumination for 60 minutes, were found to be 85.07%, 34.68%, 90.95%, 89.13%, and 46.06%, respectively. These results highlight the remarkable efficacy of our approach in degrading these small molecular pollutants (**Figure S6**).

Contribution of h^+, $\cdot O_2^-$, ·OH, and $^1O_2$ to RhB degradation. The decreased degradation kinetics by CN-8 after adding $Na_2C_2O_4$, DMPO, BQ, and DMSO into reaction system suggested that h^+, $\cdot O_2^-$, ·OH, and $^1O_2$ had contribution to RhB degradation.where α and β are the decreased degradation kinetic efficiencies and relative contribution of different reactive species to RhB degradation, respectively. k_0 is the pseudo-first-order constant for RhB degradation without scavenger as control, $k_{Na_2C_2O_4}$, k_{BQ}, k_{DMPO}, and k_{DMSO} are the pseudo-first-order constants for RhB degradation when $Na_2C_2O_4$, BQ, DMPO, and DMSO were added into the suspension, respectively(Text S2 Equation (10-17), Supporting Information).[35]

Fundamentally, Photochemical oxidation may involve different reactive species like hole (h^+), superoxide radical ($\cdot O^{2-}$), hydroxyl radical (·OH), and singlet oxygen ($^1O_2$). Supplementary Fig. 4a depicts the ESR spectra using 2,2,6,6-Tetramethylpiperidine 1-oxyl (TEMPOL) as spin-labeling agent. After 5 minutes of illumination, the ESR intensity of TEMPOL did not change, indicating that CN-8 generate photoinduced electrons under light exposure did not captured by TEMPOL. **Figure 6**d-f demonstrates that spin trapping experiments using 5,5-dimethyl-1-pyrroline N-oxide (DMPO) provide direct evidence of the formation of DMPO-$\cdot O^{2-}$ adducts (quartet, 1:1:1:1) and DMPO-·OH adducts (quartet, 1:2:2:1).[35] No EPR signal is observed when there is no DMPO or in the dark. The influence of such reactive species was validated by the use of corresponding scavengers with other identical conditions, namely, sodium oxalate (NaC_2O_4, h^+ scavenger),

benzoquinone (BQ, $\cdot O^{2-}$ scavenger), dimethylsulfoxide (DMSO, $^1O_2$ scavenger) and dimethylpyridine nitrogen oxide (DMPO, $\cdot OH$ and $\cdot O^{2-}$ scavenger) were added to reaction system in separate runs. Fig 5b and Equation (13-16) show that $\beta(h^+) = 16.36$ %, $\beta(\cdot O_2^-) = 19.59$ %, $\beta(\cdot OH) = 31.67$ % , and $\beta(^1O_2) = 32.38$ % are the decreased degradation kinetic efficiencies and relative contribution of different reactive species to RhB degradation, respectively.

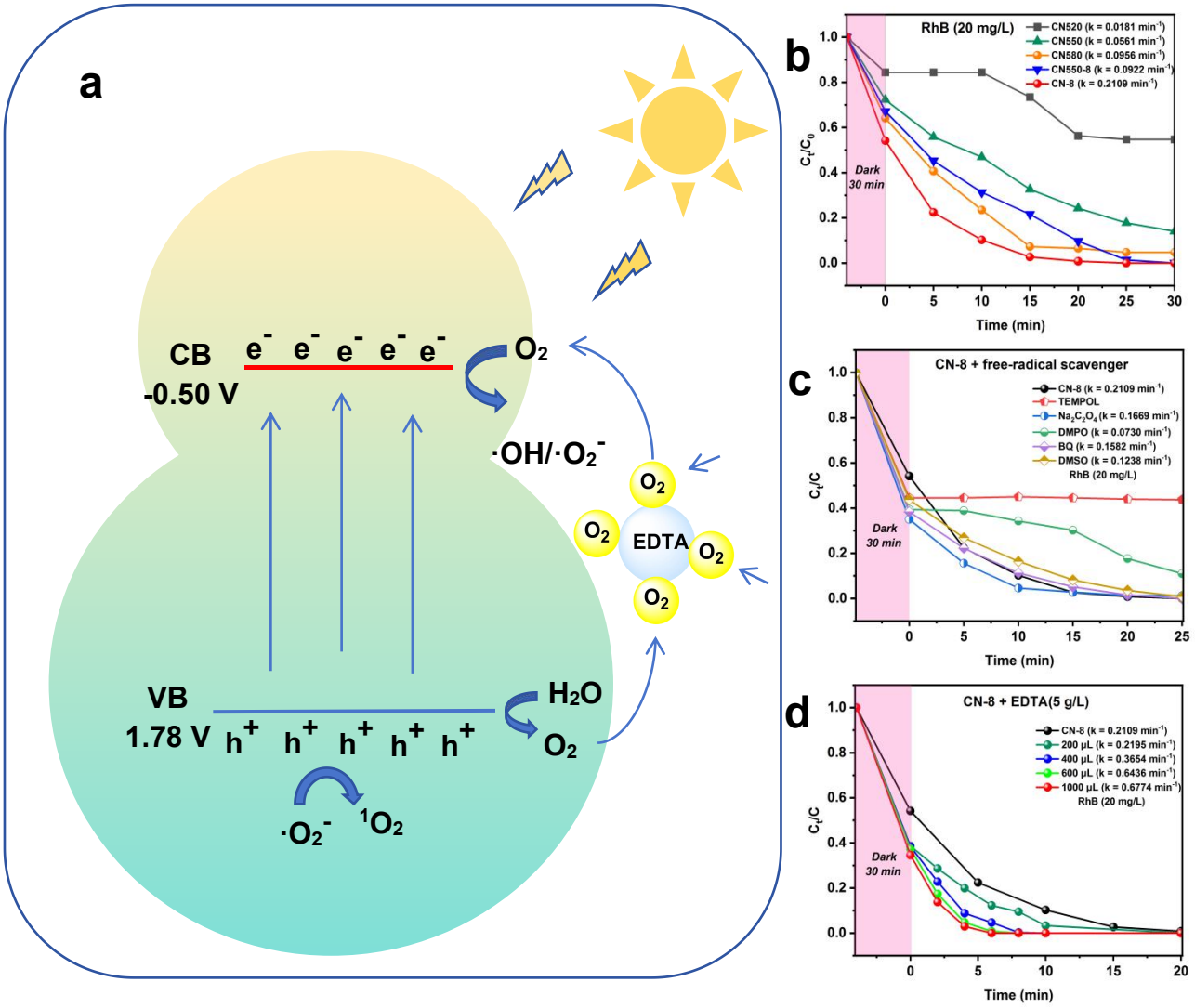

Figure 10. (a) Illustration of the charge generation, separation and transformation processes in the $O_2/\cdot O^{2-}$/EDTA/CN-8/visible-light system. (b-d) Degradation of RhB under the irradiation of a 6 W LED lamp at $\lambda = 450$ nm.

In addition, the degradation of RhB remain nearly identical after five cycles, implying our CN-8 catalyst is highly stable and recyclable (**Figure S7**). The XRD (**Figure 6**c), FT-IR (**Figure S**5) and SEM (**Figure S**9) comparisons between the original CN-8 and CN-8 after 5 cycles reveal that its corresponding structure remains intact, indicating no structural degradation of CN-8 after 5

cycles. We have further extended the reaction scope to other organic pollutants including MB, TC, BPA and FLLN.

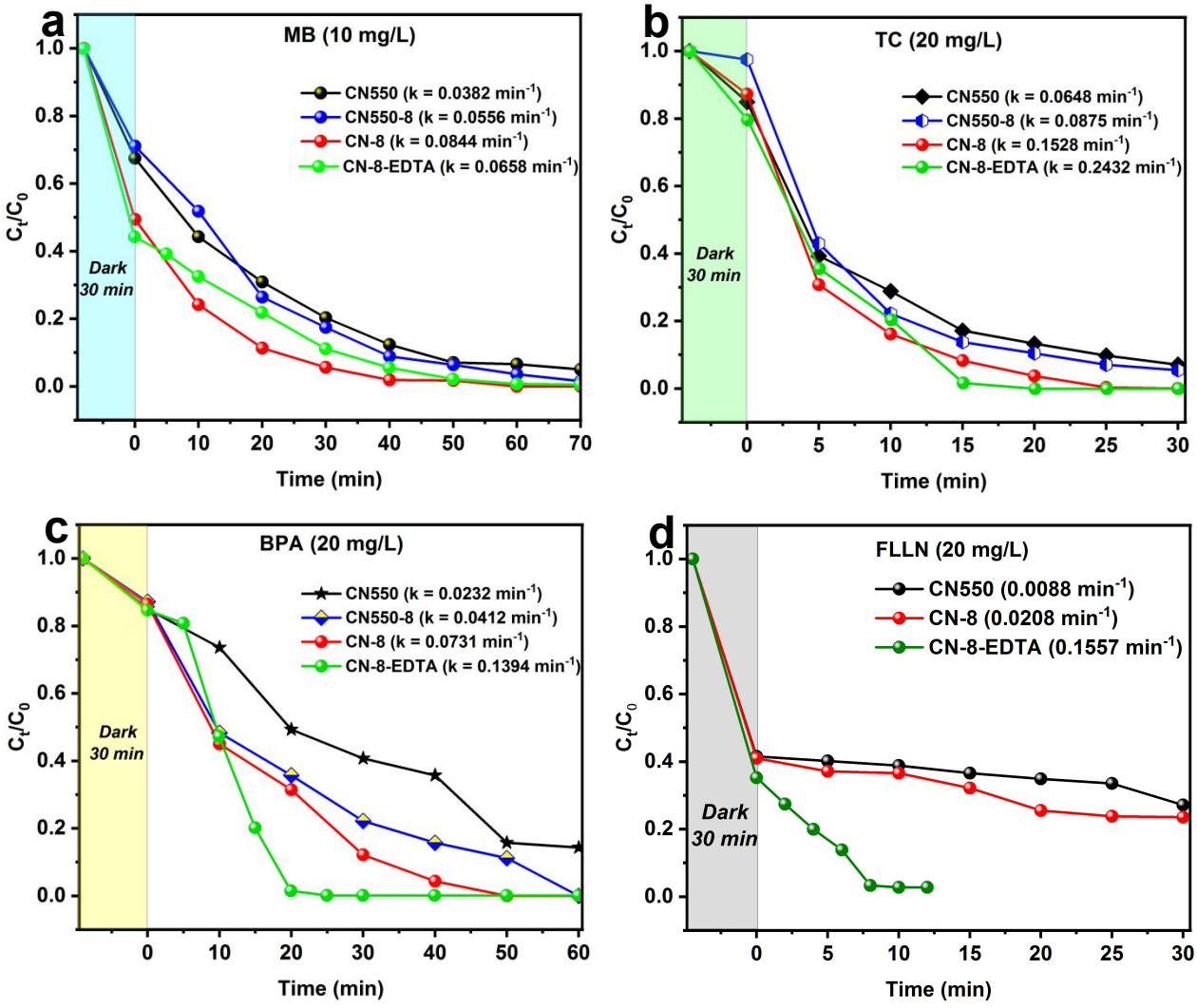

Figure 11. Degradation of MB, TC, BPA and FLLN under the irradiation of a 12 W LED lamp at λ = 450 nm.

2.4 Photocatalytic degradation test

We conducted photocatalytic degradation tests of CN-8-EDTA on RhB, MB, TC, and BPA using a catalyst concentration of 0.5 g/L. The optimal amount of EDTA was determined by screening the degradation rate of RhB, and it was found that adding more than 600 μL did not significantly enhance the degradation rate. Therefore, we chose to use 600 μL of EDTA.

Before the addition of EDTA, the first-order rate constants (*k*) of CN-8 for RhB, MB, TC, BPA and FLLN were 0.2109 min^{-1}, 0.0844 min^{-1}, 0.1528 min^{-1}, 0.0731 min^{-1} and 0.0208 min^{-1}, respectively. After adding 600 μL of EDTA, the degradation rates of RhB, TC, BPA and FLLN

increased significantly, with *k* values of 0.6436 min^{-1}, 0.2432 min^{-1}, 0.1394 min^{-1} and 0.1557 min^{-1}, respectively. However, the degradation rate of MB decreased, with a k value of 0.0658 min^{-1}.The addition of EDTA facilitated O^2 reduction through H-bonding, promoting the generation of $\cdot O^{2-}$ and $^1O^2$, thereby increasing the degradation efficiency. EDTA also acted as a scavenger for hydroxyl radicals, further enhancing the degradation process. However, in the case of MB, the reaction rate actually decreased, indicating that ·OH is the main active radical for its degradation. To further analyze the degradation of TC, BPA and FLLN, we plotted in situ trace UV-visible absorption spectra (Figure S10-12, Supporting Information). We conducted a comparative study with similar catalysts and found that the photocatalytic performance of CN-8 is at the cutting edge level (**Table S**6-9**,** Supporting Information).

3. Conclusion

In summary, we present a novel approach for modifying g-C_3N_4 using benzaldehyde compounds with various electron-donating and electron-withdrawing groups at the amino position. Through DFT calculations and experimental validation, we identified CN-8 as the most efficient compound for degradation, with a rate of 0.0844 min^{-1} towards MB. By adding EDTA, the degradation rates of RhB, TC, BPA and FLLN were significantly improved to 0.6436 min^{-1}, 0.2432 min^{-1}, 0.1394 $min^{-1}$and 0.1557 min^{-1} , respectively. Mechanistic studies confirmed that the introduction of strong electron-donating functional groups at the amino position of g-C_3N_4 enhances the separation of photogenerated charge carriers. This enhancement enables CN-8, in the presence of EDTA, to generate superoxide radicals more effectively under light conditions, thereby promoting the degradation reaction. This work provides a promising strategy for designing efficient photocatalysts for water pollutant decontamination.

4. Experimental Section

4.1 Materials and reagents

Urea, absolute ethyl alcohol, glacial acetic acid, $Na_2C_2O_4$, DMSO, DMPO, BQ, TEMPOL, RhB, MB, TC, and BPA were purchased from Macklin. 4-fluorobenzaldehyde (CN-1), 2,3-dimethylbenzaldehyde (CN-2), 3-nitrobenzaldehyde (CN-3), 4-bromobenzaldehyde (CN-4),

554 terephthalaldehyde (CN-5), 2-nitrobenzaldehyde (CN-6), 2-bromo-6-nitrobenzaldehyde (CN-7),
555 4-nitrobenzaldehyde (CN-8), 2,4-dinitrobenzaldehyde (CN-9), 3-fluoro-4-nitrobenzaldehyde
556 (CN-10), 3-methyl-4-nitrobenzaldehyde (CN-11), and 2,6-difluorobenzaldehyde (CN-12) were
557 purchased from Aladdin.
558
559 **4.2 Synthesis of pristine g-C_3N_4(CN550) and CN580**
560 The CN550 were fabricated by a typical synthesis route. In brief, urea (10.0 g) in a silica boat
561 was heated at 550 °C for 3 h using a heating rate of 10 °C min^{-1}in a muffle furnace in an air
562 atmosphere. The resulting yellow product was pulverized using an agate mortar for further
563 utilization. The synthesis of CN580 is similar to CN550, with the only difference being its
564 calcination temperature at 580 °C.
565
566 **4.3 Synthesis of CN-1~CN-12**
567 Place 0.5 g of CN580 into a 100 mL round bottom flask and add 50 mL of anhydrous ethanol.
568 Stir the mixture evenly and then add 0.1g of 4-nitrobenzaldehyde (CN-8). Reflux the solution at
569 80 °C for 12 hours. Once the reaction is complete, pour the mixture into 200 mL of ice water and
570 stir for 10 minutes. Then, filter it, rinse it three times with distilled water, followed by three rinses
571 with anhydrous ethanol.[31] Dry the product in an 80 °C oven for 2 hours and grind it into powder
572 using an agate mortar. CN-1 to CN-12 are all prepared using this method with different
573 benzaldehyde compounds.
574
575 **4.4 Material characterizations**
576 The morphology and structure of the samples were characterized by SEM(FEI Nova
577 NanoSEM450), TEM (FEI Talos F200C), and HRTEM. X-ray diffraction (XRD) (Japan Rikagu
578 Ultima IV). X-ray photoelectron spectroscopy was performed using a Thermo SCIENTIFIC
579 ESCALAB 250Xi system . All binding energies were calibrated by using the contaminant carbon
580 (C 1 s = 284.8 eV) as a reference. Fourier transform infrared (FTIR) spectra were obtained on
581 Thermo Fisher iS5. The Bruker EMXPlus used for ESR testing. The full pore was tested using the
582 Micromeritics ASAP2460 from the United States. Diffuse reflectance absorption testing was
583 conducted using the UH4150 instrument. Photocurrent correlation testing was performed using the

CHI660e instrument from China-Shanghai Chenhua. PL testing was conducted using the Hitachi F-4700. The electronic transient lifetime was measured using the Horiba Fluorolog-QM steady-state and transient fluorescence phosphorescence spectrometer. The Raman spectroscopy tests using the Thermo DXR2xi instrument from the renowned American company, Thermo Fisher Scientific. The LC-MS tested by the U3000 system from the renowned American company, Thermo Fisher Scientific.The TOC (Total Organic Carbon) testing using the varioTOC select instrument from the renowned German company, Elementar.

4.5 Computational methods

All DFT calculations were performed using Gaussian 09 software. The method chosen for structure optimization was DFT-(B3LYP) with a basis set of 6-31G. The single-point energy calculations were performed using TD-DFT-(CAM-B3LYP) with a basis set of 6-31G' d. The data obtained from DFT calculations were processed using Multiwfn software.

4.6 Photocatalytic degradation experiment

The photocatalytic degradation experiments were conducted using the PL-SX100A multi-channel photocatalytic reaction instrument. Visible light with a wavelength of $\lambda = 450$ nm was selected, and the volume of the degradation solution was 10 mL. The catalyst dosage was 0.5 g/L, and the experiments were conducted in parallel in 3 groups, with the average values taken. For testing RhB, the LED light intensity selected was 6 W, while for testing MB, TC, and BPA, the LED light intensity selected was 12 W. The absorbance values of RhB and MB were measured using the BioTek uQuant full-wavelength microplate reader. The TC and BPA were measured using the Thermo Fisher NanoDrop One microvolume UV-Vis spectrophotometer.

4.7 Regression analysis

We used Origin Pro 2022 software to analyze the measured results. The iterations were conducted until a Chi-square tolerance of 1×10^{-9} was reached, and the fits were iterated until at least 95% of the data matched the model ($R^2 > 0.95$).

Supporting Information

Supporting Information is available from the Wiley Online Library or from the author.

Acknowledgements

This work was supported by National Ten Thousand Talents Plan and the high performance computing platform of Guizhou University. The financial support from the Program of Introducing Talents to Chinese Universities (No. D20023), the Guiding Funds of Central Government, Guizhou province [Qiankehezhongyindi(2023)001], the Innovation Platform for Academicians of Hainan Province (SQ2020PTZ0009) were also appreciated.

Author contributions

Hong Tu designed and performed the experiments, collected and analyzed the data, and wrote the manuscript. Yao Tang helped toperformed the experiments. Renjiang Guo and Shengxin Guo help to helped toperformed the experiments. Yin Xu help to helped toperformed the experiments. Shunhong Chen, Ya Wang, and Yaming Liu helped to analyze the data. Jian Wu conceived the project, analyzed the data, and improved the manuscript.

Competing interests

The authors declare that they have no competing interests.

References

[1] M. Carere, A. Antoccia, A. Buschini, G. Frenzilli, F. Marcon, C. Andreoli, G. Gorbi, A. Suppa, S. Montalbano, V. Prota, F. De Battistis, P. Guidi, M. Bernardeschi, M. Palumbo, V. Scarcelli, M. Colasanti, V. D'Ezio, T. Persichini, M. Scalici, A. Sgura, F. Spani, I. Udroiu, M. Valenzuela, I. Lacchetti, K. di Domenico, W. Cristiano, V. Marra, A. M. Ingelido, N. Iacovella, E. De Felip, R. Massei, L. Mancini, *J Environ Manage* **2021**, 300, 113549.

[2] N. Haffiez, T. H. Chung, B. S. Zakaria, M. Shahidi, S. Mezbahuddin, F. I. Hai, B. R. Dhar, *Bioresour Technol* **2022**, 354, 127189.

[3] M. Edwin Malefane, P. John Mafa, T. Thokozani Innocent Nkambule, M. Elizabeth Managa, A. Tawanda Kuvarega, *Chemical Engineering Journal* **2023**, 452.

[4] M. Sharma, K. Kumar, K. K. Dubey, *Environmental Quality Management* **2021**, 30, 127.

[5] P. J. Mafa, M. E. Malefane, F. Opoku, A. Sacko, A. O. Oladipo, S. L. Lebelo, D. Liu, J. Gui, B. B. Mamba, A. T. Kuvarega, *Journal of Cleaner Production* **2023**, 429.

[6] L. Chen, M.-L. Tsai, Y. Chuang, C.-W. Chen, C.-D. Dong, *Carbon* **2022**, 196, 877.

[7] P. J. Mafa, M. E. Malefane, F. Opoku, B. B. Mamba, A. T. Kuvarega, *Chemical Engineering Journal* **2023**, 464.

[8] C. W. Sheng, Q. T. Huang, G. Y. Liu, X. X. Ren, J. Jiang, Z. Q. Jia, Z. J. Han, C. Q. Zhao, *Pest Management Science* **2019**, 75, 2901.

[9] C. Wells, C. M. T. Collins, *Environmental Science and Pollution Research* **2022**, 29, 45070.

[10] A. Tkaczyk, K. Mitrowska, A. Posyniak, *Science of The Total Environment* **2020**, 717.

[11] M. K. Shahid, A. Kashif, A. Fuwad, Y. Choi, *Coordination Chemistry Reviews* **2021**, 442.

[12] M. E. Malefane, P. J. Mafa, M. Managa, T. T. I. Nkambule, A. T. Kuvarega, *The Journal of Physical Chemistry Letters* **2023**, 14, 1029.

[13] G. Liao, Y. Gong, L. Zhang, H. Gao, G.-J. Yang, B. Fang, *Energy & Environmental Science* **2019**, 12, 2080.

[14] F. K. Kessler, Y. Zheng, D. Schwarz, C. Merschjann, W. Schnick, X. Wang, M. J. Bojdys, *Nature Reviews Materials* **2017**, 2.

[15] Y. Li, Z. He, L. Liu, Y. Jiang, W.-J. Ong, Y. Duan, W. Ho, F. Dong, *Nano Energy* **2023**, 105.

[16] Q. Xu, Z. Xia, J. Zhang, Z. Wei, Q. Guo, H. Jin, H. Tang, S. Li, X. Pan, Z. Su, S. Wang, *Carbon Energy* **2022**, 5.

[17] R. Zou, Z. Chen, L. Zhong, W. Yang, T. Li, J. Gan, Y. Yang, Z. Chen, H. Lai, X. Li, C. Liu, S. Admassie, E. I. Iwuoha, J. Lu, X. Peng, *Advanced Functional Materials* **2023**, 33.

[18] Y. Hou, F. Liu, B. Zhang, M. Tong, *Environmental Science & Technology* **2022**, 56, 16303.

[19] N. Wang, L. Cheng, Y. Liao, Q. Xiang, *Small* **2023**, 19.

[20] T. Lu, F. Chen, *Journal of Computational Chemistry* **2011**, 33, 580.

[21] Z. Liu, T. Lu, Q. Chen, *Carbon* **2020**, 165, 461.

[22] J. Dong, Y. Zhang, M. I. Hussain, W. Zhou, Y. Chen, L.-N. Wang, *Nanomaterials* **2021**, 12.

[23] B. P. Mishra, K. Parida, *Journal of Materials Chemistry A* **2021**, 9, 10039.

[24] H. Tu, S. Q. Wu, X. Q. Li, Z. C. Wan, J. L. Wan, K. Tian, G. P. Ouyang, *Journal of Heterocyclic Chemistry* **2017**, 55, 269.

[25] A. Maréchal, P. R. Rich, *Proceedings of the National Academy of Sciences* **2011**, 108, 8634.

[26] Z. Zhao, T. Yu, Y. Miao, X. Zhao, *Electrochimica Acta* **2018**, 270, 30.

[27] L. Du, B. Gao, S. Xu, Q. Xu, *Nature Communications* **2023**, 14.

[28] K. Li, X. Xie, W.-D. Zhang, *Carbon* **2016**, 110, 356.

[29] M. Song, Y. Wu, C. Xu, X. Wang, Y. Su, *Journal of Hazardous Materials* **2019**, 368, 530.

[30] K. Li, Y. Jiang, W. Rao, Y. Li, X. Liu, J. Zhang, X. Xu, K. Lin, *Chemical Engineering Journal* **2022**, 431.

[31] Y. Zhang, C. Zhang, Y. Li, P. Xu, Z. Sun, C. Zhuang, *Chemical Engineering Journal* **2023**, 474.

[32] J. Bian, Q. Li, C. Huang, J. Li, Y. Guo, M. Zaw, R.-Q. Zhang, *Nano Energy* **2015**, 15, 353.

[33] Q. Zheng, D. P. Durkin, J. E. Elenewski, Y. Sun, N. A. Banek, L. Hua, H. Chen, M. J. Wagner, W. Zhang, D. Shuai, *Environmental Science & Technology* **2016**, 50, 12938.

[34] L. Jiang, X. Yuan, G. Zeng, J. Liang, X. Chen, H. Yu, H. Wang, Z. Wu, J. Zhang, T. Xiong, *Applied Catalysis B: Environmental* **2018**, 227, 376.

[35] L. Wang, Y. Fu, Q. Li, Z. Wang, *Environmental Science & Technology* **2022**, 56, 8796.

690

691

692

693

694

695 **Table of Contents**

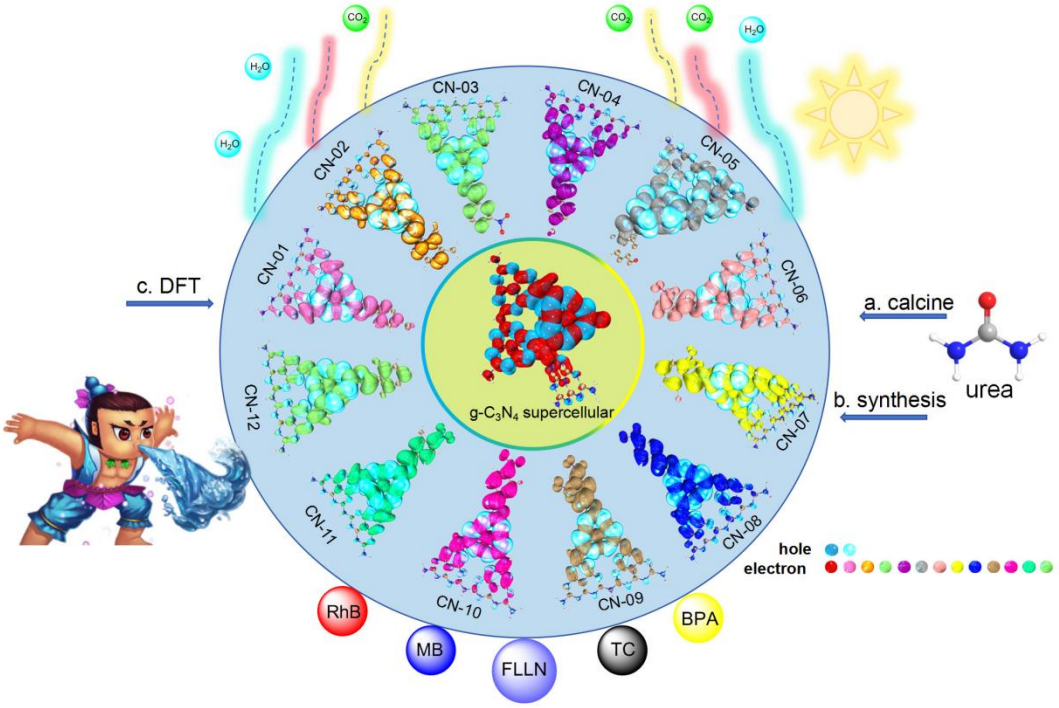

696

697 (a) Urea was calcined and (b) then the CN series was synthesized by condensing amino groups with different

698 benzaldehyde compounds. (c) DFT calculations determined the single-point energy and revealed the electron hole

699 distribution in the first excited state. The CN series exhibited degradation activity under visible light with water as

700 the solvent for RhB, MB, TC, BPA and FLLN.

701

702